Supplemental Information

Stepwise Nitrosylation of the Nonheme Iron Site in an Engineered Azurin and a Molecular Basis for Nitric Oxide Signaling Mediated by Nonheme Iron Proteins

Shiliang Tian,[1,#] Ruixi Fan,[2,#] Therese Albert,[3] Rahul L. Khade,[4] Huiguang Dai,[1] Kevin A. Harnden,[1] Parisa Hosseinzadeh,[5] Jing Liu,[1] Mark J. Nilges,[6] Yong Zhang,[4,*] Pierre Moënne-Loccoz,[3,*] Yisong Guo,[2,*] and Yi Lu[1,*]

[1]Department of Chemistry, University of Illinois at Urbana-Champaign, Urbana, IL 61801, USA
[2]Department of Chemistry, Carnegie Mellon University, Pittsburgh, Pennsylvania 15213, USA
[3]Department of Chemical Physiology and Biochemistry, Oregon Health & Science University, Portland, Oregon 97239, USA.
[4]Department of Chemistry and Chemical Biology, Stevens Institute of Technology, Hoboken, NJ 07030, USA.
[5]Department of Biochemistry, University of Illinois at Urbana-Champaign, Urbana, IL 61801, USA
[6]School of Chemical Sciences Electron Paramagnetic Resonance Lab, University of Illinois at Urbana-Champaign, Urbana, IL 61801, USA
[#]S.T. and R.F. contributed equally to this work

Materials. $(NH_4)_2Fe(SO_4)_2$, Na_2IrCl_6, dithionite and chelex-100 sodium form were purchased from Sigma-Aldrich Chemical Co. and used without further purification. All the primers for site-directed mutagenesis were purchased from IDT Inc. and used without further purification. DEA and PROLI NONOates were purchased from Cayman Chemical Co. and used without further purification. The water used in all experiments was purified by a Milli-Q system (Millipore, Bedford, MA, USA). All buffers were incubated with Chelex-100 beads and filtered through a Millipore 0.2 μm filter membrane before use. All other chemicals were purchased from Fisher Scientific Inc. and used without further purification.

Site-directed Mutagenesis and Protein Purification. Plasmid containing the M121H/H46E mutations was constructed by site-directed mutagenesis using wild-type azurin (pET9a) as the template for the quick change mutagenesis procedure with the forward primers 5'-CGA AGA ACG TTA TGG GTG AAA ACT GGG TTC TGT CC-3' (fwd-H46E), 5'-CAC TCC GCA CTG CAT AAA GGT ACC CTG-3' (fwd-M121H) and the reverse primers 5'-GGA CAG AAC CCA GTT TTC ACC CAT AAC GTT CTT CG-3' (rev-H46E), 5'-CAG-GGT-ACC-TTT-ATG-CAG-TGC-GGA-GTG-3' (rev-M121H). The mutations were confirmed by sequencing. The protein was expressed in BL-21* *E. Coli* (Novagen, Madison, WI) and purified according to published procedures.[1] Electrospray ionization mass spectrometry confirmed the identity of the isolated variant (apo-M121H/H46EAz, $MW_{obs} = 13944$, $MW_{cal} = 13943.73$).

UV-vis Spectroscopy Measurements. UV-vis absorption spectra were obtained at room temperature on an HP Agilent 8453 diode array spectrometer. Extinction coefficient of 9000 $M^{-1}cm^{-1}$ at 280 nm was used to determine apo protein concentration. All UV-vis spectra were recorded in 50 mM Bis(2-hydroxyethyl)-amino-tris(hydroxymethyl)-methane (BisTris) buffer pH 7.0 unless otherwise stated. Singular value decomposition (SVD) analysis on the time dependent optical absorption spectra was carried out by using KinTek Global Kinetic Explorer Version 10 [2-3] with the established procedure.[4] Briefly, the time dependent optical absorption spectra were first subject to singular value decomposition. The first three or four SVD components were selected for further kinetic analysis. The kinetic model included in Figure S17 were used to simulate the time-dependent traces of the selected SVD components. Based on the kinetic simulations, the optical absorption spectra of the potential physical species as well as the time dependent changes of these species were reconstructed. Finally, the rate constants derived from the kinetic analysis on the SVD components were used to simulate the kinetic traces at 720 nm obtained from the initial time dependent optical absorption spectra.

Mass Spectrometry Measurements. The mass spectra of the proteins were acquired using a Waters Quattro II spectrometer operating in positive-ion mode. Samples (10 μL of 50 μM protein in 50 mM ammonium acetate buffer at pH 6.0) were injected into a flow of 50 μL/min of 50% CH_3CN/H_2O mobile phase. The mass spectra were collected from 500 to 2000 m/z and deconvoluted using the MassLinx software package with a 1 Da resolution and a 10,000 – 20,000 Da calculation window.

Electron Paramagnetic Resonance (EPR) Spectroscopy Measurements. All the EPR samples are prepared with natural abundance Fe. X-band EPR spectra were collected on a Varian-122 spectrometer equipped with an Air Products Helitran cryostat, EIP frequency counter and temperature controller with a collection frequency of 9.20 ~ 9.55 GHz, power of 0.2 mW and field modulation of 4.0 G. Samples for EPR were typically 0.4 mM in 50 mM BisTris pH 7.0 buffer. Pulsed ENDOR spectra were obtained on a Bruker ElexSys E-580-10 FT-EPR Q-band EPR spectrometer using an ENI A 300RF amplifier and an Oxford Instruments CF935 cryostat at 30 K. Davies pulsed ENDOR experiments were carried out using a three pulse scheme (π_{mw}-T-$\pi/2_{mw}$-τ-π_{mw}-τ-echo, π_{rf} was applied during T). Samples for ENDOR spectroscopy were 2.0 mM protein in 50 mM BisTris pH7.0 buffer.

Resonance Raman spectroscopy measurements. Resonance Raman (RR) spectra of complexes **1** and **2** (1.5 mM final protein concentration in 50 mM Bis-Tris buffer pH 7.0), were collected at room temperature using a 90° scattering geometry with a McPherson 2061/207 spectrograph equipped with a liquid nitrogen cooled CCD detector (LN-1100PB, Princeton instruments). The 457-nm laser line from a Ar laser (Innova 90, Coherent) was used as the excitation wavelength and was maintained below 20 mW at the samples. A long-pass filter (RazorEdge, Semrock) was used to attenuate the Rayleigh scattering. The samples integrity was confirmed by collecting UV-vis spectra of the samples inside the Raman capillaries before and after exposure to the laser emission. Photosensitivity of the NO adducts was also assessed by collecting rapid acquisitions with minimal laser power and continuous sample translation to compare with longer data acquisition on static samples. Total acquisition times between 15 and 20 minutes were sufficient to produce high-quality RR spectra. Frequencies were calibrated with indene and CD_3CN and are accurate to ± 1 cm^{1}.

FTIR spectroscopy measurements. FTIR films were prepared inside an anaerobic glovebox by loading solutions between two CaF_2 windows separated by a 25 μm Teflon spacer. The protein final concentration was 3.5 mM and that of DEA-NONOate was 5 mM to produce a total of 2 equiv NO per iron center. Experiments with higher DEA-NONOate concentrations resulted in excessive build-up of NO beyond solubility and resulted in microbubble formation which adversely affected the quality of the FTIR transmittance spectra. All solutions were prepared using D_2O in order to monitor N-O stretching vibrations without the overlapping H-O-H bending mode of water at 1645 cm^{-1}. The solutions, windows, and cell holders were pre-cooled to 10 °C to slow down the decay rate of DEA-NONOate and allow the collection of initial FTIR spectra with minimal formation of complex **1**. A 22-µL droplet of the protein solution was laid in the center of the first CaF_2 window before adding 2.5 µL of a DEA-NONOate stock solution and placing the second CaF_2 window on the droplet to form the IR film. The chilled cell was rapidly taken outside of the glovebox and transferred inside the sample chamber of a Vertex 80 Bruker FTIR spectrograph. Constant purging of the chamber with dry air contributed to the rise of the cell temperature to room temperature within 6 min. FTIR spectra were collected as 1000-scan accumulation with a 4-cm^{-1} resolution.

Fe(II) Titration. Apo M121H/H46EAz in 25 mM Tris buffer pH 7.8 was degassed in a Schlenk line and transferred to an anaerobic chamber (Coy Laboratories). Aliquots of degassed $(NH_4)_2Fe(SO_4)_2$ stock solution with known concentration were added to a solution containing 1 ml of 468 µM apo M121H/H46EAz in 25 mM Tris pH 7.8. UV-vis absorption spectra were recorded on an HP Agilent 8453 diode array spectrometer inside anaerobic chamber. Spectra were corrected for dilution and baseline. The dissociation constant (K_D) is determined by fitting the plot of absorbance at 330 nm as a function of Fe(II) concentration using the following equation:

$$A = A_{max} \times \{[(P + M + K_D) - [(P + M + K_D)^2 - (4 \times P \times M)]^{\frac{1}{2}}\} \div (2 \times P)$$

where P = protein concentration, M = Fe^{2+} concentration and K_D = dissociation constant. A dissociation constant (K_d) of 8.1 ± 1.0 µM was obtained.

Determination of Extinction Coefficient of Fe(II)-M121H/H46EAz. Apo M121H/H46EAz in 25 mM Tris buffer pH 7.8 was degassed in a Schlenk line and transferred to an anaerobic chamber (Coy Laboratories). Aliquots of degassed $(NH_4)_2Fe(SO_4)_2$ stock solution with known concentration were added to a solution containing 1 ml of 1.2 mM apo M121H/H46EAz in 25 mM Tris pH 7.8 with a final concentration of Fe(II) less than 500 µM in the end. UV-vis absorption spectra were recorded on an HP Agilent 8453 diode array spectrometer inside anaerobic chamber. Spectra were corrected for dilution and baseline. Based on the relatively small K_D of Fe(II)-M121H/H46E and the presence of excess apo M121H/H46EAz in solution, we correlated the concentration of Fe(II)-M121H/H46EAz with the concentration of Fe(II) added. An extinction coefficient for Fe(II)-M121H/H46EAz at 330 nm is determined by fitting the plot of absorbance at 330 nm as a function of Fe(II) concentration using Beer's law A = ε*l*c where *l* = 1 cm and c = Fe(II) concentration. An extinction coefficient (ε) of 971 ± 6 $M^{-1}cm^{-1}$ was obtained.

Preparation of Fe(II)-M121H/H46EAz. Apo M121H/H46EAz in 25 mM Tris buffer pH 7.8 was degassed in a Schlenk line and transferred to an anaerobic chamber (Coy Laboratories). Two equivalents of $(NH_4)_2Fe(SO_4)_2$ from 50 mM degassed stock solution were slowly added into the protein solution during stirring. After stirring for 30 minutes, the mixture was run down through a PD-10 desalting column (pre-equilibrated with 50 mM BisTris pH 7.0 buffer) to remove excess Fe(II). The extinction coefficient of 971 $M^{-1}cm^{-1}$ at 330 nm was used to determine the concentration of Fe(II) incorporated protein.

Preparation of $\{FeNO\}^7$. To 1.0 ml of 0.2 mM Fe(II)-M121H/H46EAz solution, 0.5 eq. Proli NONOate (from 50 mM Proli NONOate stock solution in 10 mM NaOH) was added at room temperature under stirring. The color of the solution changed from colorless to light yellow in 1 minute. The process is monitored with UV-vis spectroscopy by HP Agilent 8453 diode array spectrometer.

Preparation of $\{Fe(NO)_2\}^9$. To 1.0 ml of 0.5 mM Fe(II)-M121H/H46EAz solution, 2 eq. Proli NONOate (from 50 mM Proli NONOate stock solution in 10 mM NaOH) was added at room temperature under stirring. The process is monitored with UV-vis spectroscopy by HP Agilent 8453 diode array spectrometer.

Freeze-quench Mössbauer Experiment. Freeze-quench experiments were performed using a KinTek quench-flow instrument. An NO-saturated buffer solution (~2 mM NO in a 50 mM Tris-HCl, pH 7.5 prepared by using Proli NONOate) buffer solution was rapidly mixed with an equal volume of an oxygen-free solution containing ^{57}Fe(II)-M121H/H46EAz (1 mM) to initiate the reaction at 5 °C. The resulting reaction was terminated by injection of the solution into liquid ethane maintained at 90 K at various time points. The resulting samples were first pumped to remove liquid ethane. Then the dry frozen solution powder was packed into in-house designed freeze quench Mössbauer sample cups at 77 K to generate Mössbauer samples. The reaction time of a freeze-quenched sample is the sum of the aging time and the quench time. The aging time was the transit time for the reaction mixture through the aging hose. The quench time corresponded to the time required after injection into the cryosolvent for the reaction mixture to be cooled sufficiently to prevent further reaction and was estimated to be ~ 5 ms.

Low Temperature Cryogenic Radiolytic Reduction. Frozen samples containing ^{57}Fe enriched M121H/H46EAz containing $\{FeNO\}^7$ species suitable for Mössbauer spectroscopy were irradiated in the γ-irradiation facility of the Breazeale nuclear reactor at the Pennsylvania State University using a ^{60}Co-source. A total dose of ca. 3 Mrad was delivered. During the γ-irradiation, the sample was kept in liquid nitrogen (T = 77 K).

Mössbauer Spectroscopy. All the Mössbauer samples are prepared with isotopically enriched ^{57}Fe. Mössbauer spectra were recorded with two spectrometers equipped with constant acceleration velocity transducers that use 60 mCi ^{57}Co/Rh γ-ray sources, and Janis Research (Wilmington, MA) SuperVaritemp dewars that allow studies in applied magnetic fields of up to 8 T in the temperature range from 1.5 to 200 K. A LakeShore Model 331A temperature controller was used to control the temperature in experiments. Mössbauer spectral simulations were performed using the WMOSS software package (SEE Co, Edina. Minnesota). Isomer shifts are quoted relative to α-Fe metal at 298 K. The spectra were plotted by SpinCount developed by Prof. Michael Hendrich at Carnegie Mellon University .[5] For the simulations of $\{FeNO\}^7$ species, an S = 3/2 spin Hamiltonian is utilized, which is expressed as:

$$\hat{H} = D\left[\left(\hat{S}_z^2 - \frac{15}{12}\right) + \frac{E}{D}\left(\hat{S}_x^2 - \hat{S}_y^2\right)\right] + \beta\hat{S}\cdot g\cdot\vec{B} + \hat{S}\cdot A\cdot\hat{I} - g_n\beta_n\vec{B}\cdot\hat{I} + \hat{H}_Q$$

$$\hat{H}_Q = \frac{eQV_{zz}}{12}\left[\hat{I}_z^2 - \frac{15}{4} + \eta\left(\hat{I}_x^2 - \hat{I}_y^2\right)\right]$$

where D and E are the axial and rhombic zero-field splitting (ZFS) parameters, $\vec{B}$ represents the applied magnetic field, $\hat{I}$ is the nuclear spin of ^{57}Fe, $\boldsymbol{A}$ is the magnetic hyperfine tensor, V_{zz} is the largest principal component of the electric field gradient (EFG) tensor, Q is the ^{57}Fe nuclear excited state quadrupole moment, and η (=(V_{xx}-V_{yy})/V_{zz}) is the asymmetric parameter. For the simulations of $\{Fe(NO)_2\}^9$ species, a similar spin Hamiltonian as the one described above but without the zero field splitting terms is used.

^{57}Fe(II)-M121H/H46EAz was prepared according to the procedure described above except using $^{57}FeCl_2$ instead of $(NH_4)_2Fe(SO_4)_2$. Mössbauer samples were flash frozen in liquid nitrogen without adding glycerol.

Comments on EPR and Mössbauer analysis of $\{Fe(NO)_2\}^9$ species. A sample enriched with $\{Fe(NO)\}^9$ exhibited two Mössbauer spectral components. One was from the Fe(II)-M121H/H46EAz complex, representing ~30% of the iron in the sample (Fig. S12), and another was from an S = ½ species that must belong to the $\{Fe(NO)\}^9$ species, representing ~ 70% of the iron. Indeed, the spectral simulations on 4.2 K Mössbauer spectra collected under multiple field conditions (Fig. S11) revealed that the latter Mössbauer signal can be satisfactorily simulated by an S = ½ spin system with Mössbauer parameters resembling those of the reported $\{Fe(NO)_2\}^9$ species in the literature (Table S1).

Calculations of Mössbauer properties. The ^{57}Fe quadrupole splitting arises from the non-spherical nuclear charge distribution in the I*=3/2 excited state in the presence of an electric field gradient at the ^{57}Fe nucleus, while the isomer shift arises from differences in the electron density at the nucleus between the absorber (the molecule or system of interest) and a reference compound (usually α-Fe at 300K). The former effect is related to the components of the electric field gradient (EFG) tensor at the nucleus as follows:[6]

$$\Delta E_Q = \frac{1}{2} eQV_{zz}\left(1 + \frac{\eta^2}{3}\right)^{1/2} \tag{1}$$

where e is the electron charge, Q is the quadrupole moment of the E*=14.4 keV excited state, and the principal components of the EFG tensor are labeled according to the convention:

$$|V_{zz}|>|V_{yy}|>|V_{xx}| \quad (2)$$

with the asymmetry parameter being given by:

$$\eta = \frac{V_{xx} - V_{yy}}{V_{zz}} \quad (3)$$

The isomer shift in ^{57}Fe Mössbauer spectroscopy is given by:[7]

$$\delta_{\mathrm{Fe}} = E_A - E_{\mathrm{Fe}} = \frac{2\pi}{3} Ze^2 (<R^2>*-<R^2>)\left(|\psi(0)|_A^2 - |\psi(0)|_{\mathrm{Fe}}^2\right) \quad (4)$$

where Z represents the atomic number of the nucleus of interest (iron) and R, R* are average nuclear radii of the ground and excited states of ^{57}Fe. Since $|\psi(0)|_{\mathrm{Fe}}^2$ is a constant, the isomer shift (from Fe) can be written as:

$$\delta_{\mathrm{Fe}} = \alpha\ [\rho(0) - c] \quad (5)$$

where α is the so-called calibration constant and $\rho(0)$ is the computed charge density at the iron nucleus. Both α and c can be obtained from the correlation between experimental δ_{Fe} values and the corresponding computed $\rho(0)$ data in a training set. Then, one can use equation (5) to predict δ_{Fe} for a new molecule from its computed $\rho(0)$, basically as described in detail elsewhere for a wide variety of heme and other model systems.[7] The hybrid functional B3LYP[8] with a Wachter's basis for Fe,[9] 6-311G* for all the other heavy atoms and 6-31G* for hydrogens was used to predict Mössbauer quadrupole splittings and isomer shifts, the same approach used in the previous work for >50 iron-containing proteins and models with experiment-versus-theory linear correlation coefficients R^2=0.98 and 0.97, respectively.[6-7, 10-19] These systems cover a broad range of iron systems, including all iron spin states and all coordination states. To calculate ΔE_Q, we first evaluated the principal components of the electric field gradient tensor at the ^{57}Fe nucleus (V_{ii}), then we used equation (1) to deduce ΔE_Q, using a precise recent determination of $Q = 0.16\ (\pm 5\%) \times 10^{-28}\mathrm{m}^2$,[20] a value previously found to permit excellent accord between theory and experiment in a broad range of systems.[6-7, 10-19] To calculate δ_{Fe} values, we read the Kohn-Sham orbitals from the *Gaussian 09*[21] results into the AIM 2000 program,[22] to evaluate the charge density at the iron nucleus, $\rho(0)$. Then, we evaluated the isomer shifts by using the equation derived previously:[7]

$$\delta_{\mathrm{Fe}} = -0.404\ [\rho(0) - 11614.16] \quad (6)$$

All the quantum chemical calculations were performed using *Gaussian 09*.[21]

As there are no X-ray structures of the studied iron proteins in this work, we used geometry-optimized models to investigate their Mössbauer properties. The related Cu-containing azurin mutant x-ray structure (PDB ID: 4WKX) was used to build corresponding Fe-containing models by replacement of Cu with Fe, since previous work shows that the Fe-containing non-heme site and Cu-containing non-heme site in similar biosynthetic systems are quite similar.[23] There are two chains in this protein and the following study is focused on models built from Chain A, with a few calculations in the end of this section to show that models built from Chain B yield basically the same results. To account for the protein environment effect to a reasonable extent, based on the previous quantum chemical investigations of various metalloprotein models,[24-30] we kept the ligands around the metal center, with these protein residues modeled up to the backbone Cα positions which are fixed at the X-ray crystal structure positions to mimic protein environment. All other atomic positions were allowed to be optimized, using the BPW91 method[31-32] with the same basis described above, which was used previously in structural investigations for a number of iron proteins.[12, 18, 33-36] In addition, frequency calculations were performed at the same level to provide zero-point energy corrected electronic energies (E_{ZPE}'s), enthalpies (H's), and Gibbs free energies (G's) at 1 atm and room temperature to estimate the energy changes along possible reaction pathways, and electronic energies were further corrected by using the PCM method[37] with a solvent dielectric constant of 20 to simulate the bulk environment effect on this active site that is close to protein surface as done for similar metalloproteins.[38]

All of the iron-containing systems with experimental Mössbauer data were investigated to help reveal possible structural models. Here, because we do not have exact iron protein x-ray structures, we focused on possible first coordination shell models, without any secondary coordination spheres. This simplification may introduce some errors in calculations. Therefore, prediction errors < ~one standard deviation (σ) and occasionally < ~two standard deviations from our previous >50 calculations of isomer shifts (0.07 mm/s) and quadrupole splittings (0.3 mm/s) were accepted to help choose each structural model.[6-7, 10-19]

As shown in Table 1, regarding the NO-free iron model, the four coordinate Fe(His)$_2$(Cys)(Glu) (**A**, see Fig. 8A) has an excellent prediction of δ_{Fe} compared with the experimentally observed major species (86%), with an error of 0.05 mm/s, well within one σ. Its predicted ΔE_Q has $<2\sigma$ error. In contrast, the corresponding five coordinate model with a coordinated water as seen in other non-heme iron proteins,[12, 36] Fe(His)$_2$(Cys)(Glu)(H$_2$O) (**B**, see Fig. S1), has 1.6 σ in δ_{Fe} prediction and 1σ in ΔE_Q prediction. So, it is also likely, but is a little less probable regarding isomer shift comparison and also less probable because this does not help yield good NO-bound models as discussed below. Because the errors of isomer shift predictions for both of these models compared with the experimental minor species (14%) are well $>2\sigma$, the minor species may be due to structural heterogeneity (e.g. chain B has two different Glu conformations). Here, the Mulliken spin density ($\rho_{\alpha\beta}^{Fe}$) of ~ 4 unpaired electrons clearly show the Fe(II) high spin nature.

We then studied the S=3/2 {FeNO}^{7} models. From the starting Fe(His)$_2$(Cys)(Glu) model, three four-coordinate mononitrosyl structures could be built by replacing respectively His/Glu/Cys by the incoming NO, see Fig. 8C-E: **C** Fe(NO)(His)(Cys)(Glu), **D** Fe(NO)(His)$_2$(Cys), **E** Fe(NO)(His)$_2$(Glu). As shown in Table 1, the spin density results show that all these three models have basically the Fe(II) (S=2) center anti-ferromagnetically coupled with NO (S=1/2), in good accord with previous work of similar S=3/2 $\{FeNO\}^7$ protein and models with excellent Mössbauer property predictions.[12, 14, 36] Interestingly, for the relatively major species (40%), the $Fe(NO)(His)_2(Glu)$ model has only 0.01 mm/s error for δ_{Fe} calculation and 0.00 mm/s error for ΔE_Q prediction, both well within one σ. For the relatively minor species (30%), both Fe(NO)(His)(Cys)(Glu) (**C**) and $Fe(NO)(His)_2(Cys)$ (**D**) models have excellent isomer shift predictions (0.03 mm/s error), but the prediction error of absolute value of ΔE_Q for **C** is only half of that for **D**, although both errors are small (<~0.30 mm/s, Table 1). It should also be noted that for this species, the experimental asymmetry value is about 1.0 and thus its ΔE_Q sign is uncertain and the comparison was focused on the absolute value. In addition, we also investigated a five coordinate model, $Fe(NO)(His)_2(Cys)(Glu)$, which may be built by adding NO to the starting $Fe(His)_2(Cys)(Glu)$ species, or replacing labile water in the relatively less likely starting model of $Fe(His)_2(Cys)(Glu)(H_2O)$. However, one His (His 121, the more loosely bound His, compared to His 117) went out of the iron first coordination shell after geometry optimization, with a Fe-N distance of 5.262 Å, so it becomes effectively a four-coordinate Fe(NO)(His)(Cys)(Glu) studied above. Moreover, a six-coordinate $Fe(NO)(His)_2(Cys)(Glu)(H_2O)$ model was also studied, which may be considered by adding NO to the less likely starting model of $Fe(His)_2(Cys)(Glu)(H_2O)$. Again, this model ended up with an effectively four-coordinate Fe(NO)(His)(Cys)(Glu) studied above, with the Fe-His121 distance of 6.598 Å and Fe-water distance of 3.936 Å. These results suggest that the $\{FeNO\}^7$ complexes shall be four-coordinate, and Fe(NO)(His)(Cys)(Glu) and $Fe(NO)(His)_2(Glu)$ may be the axial and rhombic species, as detected experimentally. The negative Gibbs free energy changes as shown in Table S5 indicate that the formation of these species are thermodynamically favorable, which are consistent with experimental detection. Species **C** might be more likely than **D** to be the axial species, because its corresponding reduction product in the next step has slightly better agreement with experimental Mössbauer data (*vide infra*), and its formation is thermodynamically more favorable by ΔG of 19.74 kcal/mol, see Table S5. Other kinds of DFT methods such as B3LYP and the hybrid DFT method with dispersion correction ωB97XD[39] were also used together with a large basis set of 6-311++G(2d,2p) for all atoms to compare the formation energies between **C** and **D**, which all show the more favorable formation of **C** than **D** by ΔG of 13.64 and 10.82 kcal/mol respectively. This consistent energy trend from different computational methods is perhaps a result of less energy cost of the loss of the neutral ligand His for **C** formation than the loss of the negatively charged Glu ligand for **D** formation, since the latter involves breaking the relatively stronger electrostatic interaction between positively charged Fe and negatively charged Glu.

Before we investigated the more elusive $\{Fe(NO)_2\}^8$ or $\{FeNO\}^8$ species, we studied the $\{Fe(NO)_2\}^9$ system which has more certain experimental evidence of its coordination structure as

$Fe(NO)_2(His)(Cys)$, **F**. Indeed, for this structure, as seen from Table 1, both experimental isomer shift and quadrupole splitting were well reproduced in the calculations. As demonstrated in Fig. 9F, this two NO moieties are bent toward each other, which is similar to the NO orientations seen in x-ray structures of small dinitrosyl iron complexes.[40-41] The spin density analysis indicates basically an antiferromagnetic coupling of Fe(I) (S=3/2) with two NO radicals (S=1/2), see Table 1. In addition to this four-coordinate model, we also examined two five-coordinate models with another His or Glu added, and a six-coordinate model with both His and Glu added: $Fe(NO)_2(His)_2(Cys)$, $Fe(NO)_2(His)(Cys)(Glu)$, $Fe(NO)_2(His)_2(Cys)(Glu)$. However, during geometry optimization, the five-coordinate $Fe(NO)_2(His)_2(Cys)$ becomes effectively the four-coordinate $Fe(NO)_2(His)(Cys)$ with His121 going out of first coordination shell, similar to above studies. For the five-coordinate $Fe(NO)_2(His)(Cys)(Glu)$ and six-coordinate $Fe(NO)_2(His)_2(Cys)(Glu)$, again, during geometry optimization, all the Histidines become non-coordinated to form an effectively four-coordinate $Fe(NO)_2(Cys)(Glu)$ system, which is inconsistent with the experimental evidence of the presence of His and thus not further studied. These results together with above studies show that this protein environment strongly prefers four-coordination for iron, and the best model for the $\{Fe(NO)_2\}^9$ system is $Fe(NO)_2(His)(Cys)$, as proposed experimentally.

In principle, both $\{Fe(NO)_2\}^8$ or $\{FeNO\}^8$ species could mediate the change from the $\{FeNO\}^7$ species to the $\{Fe(NO)_2\}^9$ system. We first investigated the $\{Fe(NO)_2\}^8$ model, building from the product $\{Fe(NO)_2\}^9$ system: four-coordinate $Fe(NO)_2(His)(Cys)$. As shown in Fig. 9G, the S=1 $\{Fe(NO)_2\}^8$ model (**G**) optimized with a similar structure to its $\{Fe(NO)_2\}^9$ counterpart, with two end-on NO bent toward each other. However, both the predicted isomer shift and quadrupole splitting were quite off the experimental values, with ~4-5 σ errors, see Table 1. We then tried other possible NO orientations, including two linear NO, two NO bent away from each other, and even side-on NO. In addition, we tried different initial spin coupling setups as Fe (S=2) anti-ferromagnetically coupled to NO^- (S=1) and NO^+ (S=0), Fe (S=2) anti-ferromagnetically coupled to two NO (S=1/2). However, all of these trials ended up with the same result as for **G**, which has a spin density distribution similar to its $\{Fe(NO)_2\}^9$ counterpart, **F**, see Table 1. We then studied the S=0 state for this four-coordinate system, **H**, which, as seen from Table 1, has even worse isomer shift prediction (9σ) and still a bad quadrupole splitting prediction (>2σ). Therefore, we then examined other S=1 five- and six-coordinate models. The original His121 and Glu46 ligand in the starting non-heme iron site were respectively included to build the initial two different five-coordinate models: $Fe(NO)_2(His)_2(Cys)$ and $Fe(NO)_2(His)(Cys)(Glu)$. However, during the geometry optimization for $Fe(NO)_2(His)_2(Cys)$, the His121 again went out of iron coordination to resume the effectively four-coordinate $Fe(NO)_2(His)(Cys)$ structure studied above. In contrast, the five-coordinate $Fe(NO)_2(His)(Cys)(Glu)$ models have been successfully obtained with two NO orientations. In one structure (**I**), as demonstrated in Fig. 9I, the two NO bent toward to the same side (one is more bent with

140° ∠Fe-N-O angle, the other is less bent with 173° bond angle), which is different from the two NO bent toward each other conformation found for four-coordinate $Fe(NO)_2$(His)(Cys). Interestingly, using initially two NO bent toward each other or side-on NO also finished with this same structure after geometry optimization. In addition, using different initial spin coupling patterns as Fe (S=2) anti-ferromagnetically coupled to NO^- (S=1) and NO^+ (S=0), Fe (S=2) anti-ferromagnetically coupled to two NO (S=1/2), Fe (S=3/2) anti-ferromagnetically coupled to NO (S=1/2), NO^- (S=0), and Fe (S=5/2) anti-ferromagnetically coupled to NO^- (S=1) and NO (S=1/2)) all ended up with the same result after geometry optimization. However, using initially two NO bent away from each other was optimized as the initial conformation (**J**), see Fig. 9J. So, there are two optimized five-coordinate $Fe(NO)_2$(His)(Cys)(Glu) structures with the two NO bent toward the same side (**I**) and opposite side (**J**) respectively, both different from the two NO bent toward each other conformation found for four-coordinate $Fe(NO)_2$(His)(Cys). Their spin density distribution patterns are also different from that of the four-coordinate **G**. Unfortunately, as seen from Table 1, none of these five-coordinate structures yielded good Mössbauer data predictions, with errors of ~3-4 σ. Lastly, we tried the six-coordinate $\{Fe(NO)_2\}^8$ S=1 structure with both the original His121 and Glu46 ligands in the starting non-heme iron site added to the four-coordinate $Fe(NO)_2$(His)(Cys). Nevertheless, during the geometry optimization, His121 again lost the iron coordination, so there is no stable six-coordinate $\{Fe(NO)_2\}^8$ S=1 structure.

Since above studies show that basically all possible structures with a $\{Fe(NO)_2\}^8$ motif do not agree with experimental Mössbauer data, we then examined structures with the $\{FeNO\}^8$ motif. Because this motif differs from the four-coordinate $\{FeNO\}^7$ precursor by basically one electron and such iron proteins have been repeatedly found in the above studies to prefer the four-coordination, we evaluated three four-coordinate $\{FeNO\}^8$ models from the three four-coordinate $\{FeNO\}^7$ precursors (**C-E**) to furnish a comprehensive comparison. Interestingly, Fe(NO)(His)(Cys)(Glu) (**K**, see Fig. 9K), which could be a precursor of the $\{Fe(NO)_2\}^9$ species ($Fe(NO)_2$(His)(Cys)) and is a product of the axial $\{FeNO\}^7$ species **C**, produced only 0.05 mm/s error (< one standard deviation) in δ prediction (Expt', **3'**, Table 1), which has clearly better agreement with experiment compared with the 0.13 mm/s error (twice standard deviation) for $Fe(NO)(His)_2$(Cys) (**L**), another likely precursor for the subsequent $\{Fe(NO)_2\}^9$ species **F**. While ΔE_Q predictions for both possible precursors are in good agreement with experiment, the formation of **K** is thermodynamically more favorable than **L** by ΔG of 10.20 kcal/mol, see Table S5. The other S=1 $\{FeNO\}^8$ species (**M**) with a ligand set from the rhombic $\{FeNO\}^7$ precursor (**E**) has δ and ΔE_Q predictions close to the experimental data for species **3** (labeled as Expt in Table 1), with errors of 0.14 and 0.13 mm/s respectively. Because of the ligand set difference, this species is not involved in the formation of the subsequent $\{Fe(NO)_2\}^9$ species $Fe(NO)_2$(His)(Cys). For these elusive $\{FeNO\}^8$ intermediates, calculations with other NO conformations including both NO orientations in other inter-residue spaces and linear vs.

nonlinear Fe-N-O angles compared to the final structures shown in Fig.9 were performed, which resulted in basically the same structures.

Since the experimental Mössbauer experiment alone cannot firmly determine its spin state, the S=0 four-coordinate $\{FeNO\}^8$ complex (**N**) with the same coordination ligands as in **L**, was also investigated. However, this structure has much worse predictions for both δ_{Fe} and ΔE_Q, see Table 1, and with a higher electronic energy by 10.48 kcal/mol. Similarly, an additional S=0 structure (**O**, with the same ligand set of the S=1 **M**) again has even worse Mössbauer data predictions and higher electronic energy by 16.86 kcal/mol. So the S=0 system with the same ligand set of S=1 **K** was not calculated.

Overall, the average computational errors of the six isomer shifts and six quadrupole splittings experimentally measured for the starting Fe(II) system, the axial and rhombic $\{FeNO\}^7$ species, the axial and rhombic $\{FeNO\}^8$ species, and the $\{Fe(NO)_2\}^9$ species, are 0.06 and 0.18 mm/s respectively, well within one standard deviations of our previous >50 calculations of isomer shifts (0.07 mm/s) and quadrupole splittings (0.3 mm/s). [6-7, 10-19]

In addition to above calculations using models based on the Chain A structure, additional calculations using Chain B starting geometry for a subset of the models for the starting Fe(II) system (model **A**), the $\{FeNO\}^7$ species (model **D**), the $\{FeNO\}^8$ species (model **L**), and the $\{Fe(NO)_2\}^9$ species (model **F**) were also performed, which resulted in basically the same predictions of both Mössbauer properties with the following respective differences for δ_{Fe} and ΔE_Q: 0.01 and 0.11 mm/s for model **A**, 0.00 and 0.01 mm/s for model **D**, 0.00 and 0.04 mm/s for model **L**, and 0.00 and 0.01 mm/s for model **F**. These data further support above results. Since Chain B has one conformation with Glu not coordinated, two structures for the starting model **A** were studied. The one containing this initially non-coordinated Glu in the ligand set becomes basically the same as this model based on Chain A after geometry optimization, as indicated by 0.01 and 0.11 mm/s respective differences for δ_{Fe} and ΔE_Q and 0.012 Å difference of Fe-Glu distance. This is due to strong interaction between positively charged Fe(II) and negatively charged Glu in this isolated model. In contrast, the model without this non-coordinated Glu in the ligand set, i.e. $Fe^{II}(His)_2(Cys)$, has the predicted δ_{Fe} and ΔE_Q of 0.64 and -1.61 mm/s, which are very different from the experimentally measured Mössbauer data for both major and minor species (see Table 1) and thus suggest that this conformation was not detected in the Mössbauer experiment due possibly to different experimental conditions compared to the x-ray crystallography. However, this flexible Glu conformation does support the most favorable pathway for $\{Fe(NO)_2\}^9$ formation from the axial species as shown in Fig.10 involving the loss of Glu coordination. The more favorable formation of this axial $\{FeNO\}^8$ precursor than the rhombic one (by ΔG of 9.31 kcal/mol, see Table S5) may facilitate its subsequent transformation to the $\{Fe(NO)_2\}^9$ species. This helps qualitatively to understand only the rhombic $\{FeNO\}^8$ intermediate was observed in the chemical reduction at room temperature, while both the axial and rhombic {FeNO}^{8} intermediates were detected in the cyroreduction experiment.

Previous work shows that the quantitative effect may be small for Mössbauer parameters even with a strong hydrogen bond, like the one between O_2 and second sphere distal His residue in myoglobin with a calculated energy of ~7 kcal/mol: it only improves the calculated Mössbauer isomer shift and quadrupole splitting by 0.03 and 0.11 mm/s respectively,[17] which are about half of the average computational errors here. Here, since there are three residues (M13, N47, F114) with distances close to hydrogen bonding interactions with the first sphere coordination ligands (H121 and C112, see Fig.1b), we chose the model **(D**) that retains both H121 and C112 and thus could potentially have all these three second-sphere interactions, as an example, to evaluate their potential effects on Mössbauer property predictions. As shown in Table S6, the calculated Mössbauer isomer shift and quadrupole splitting from **D‘** which has all these three residues in addition to model **D** are affected by only 0.02 and 0.11 mm/s respectively, basically the same level of small effect as mentioned above. The influence on the predicted NO frequency is 0.4% and the calculated spin densities are changed by ~1%, which all indicate an insignificant effect. In addition, to find out if the second sphere residues could affect the Mössbauer property predictions through inducing different NO conformations, we performed calculations on the elusive {FeNO}^{8} intermediates with other NO conformations including both NO orientations in other inter-residue spaces and linear vs. nonlinear Fe-N-O angles compared to the final structures shown in Fig. 9. The calculations resulted in basically the same structures. We then conducted additional single point Mössbauer property predictions using the optimized structures but with just NO manually rotated to other inter-residue spaces (the energy cost for rotation is small, which can usually be accommodated by the protein environment). Results show that the calculated Mössbauer isomer shifts and quadrupole splittings are affected on average by 0.02 and 0.12 mm/s respectively, which are again at the same level of small effect as from hydrogen bonding mentioned above. Therefore, the second sphere residues may be unlikely to significantly alter the computed data here.

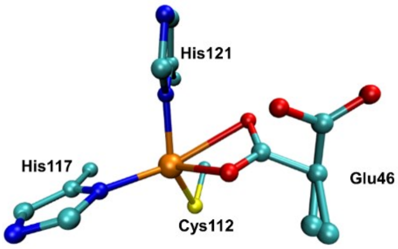

Figure S1. Metal-binding site in Cu-M121H/H46EAz (Chain B). Glu46 adopts two different conformations. (PDB: 4WKX)

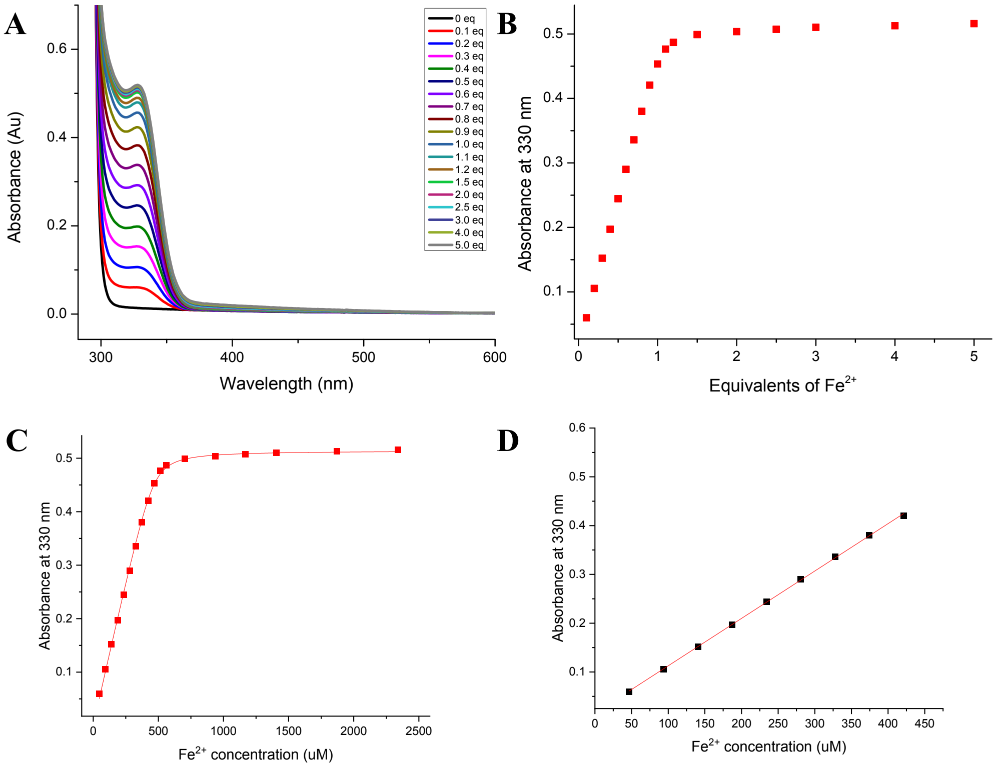

Fig. S2 | Fe^{2+} Titration of apo-M121H/H46EAz. (A) UV-vis absorption spectral of titrating 0.1 – 5.0 eq. of Fe^{2+} to apo-M121H/H46E in 50mM BisTris pH7.0. (B) Titration curve monitored by the increased absorbance at 330 nm versus the equivalents of Fe^{2+}. (C) The dissociation constant (K_D) is determined by fitting the plot of Abs at 330 nm vs. Fe^{2+} concentration using the following equation: $A = A_{max} \times \{[(P + M + K_D) - [(P + M + K_D)^2 - (4 \times P \times M)]^{\frac{1}{2}}\} \div (2 \times P)$ where P = protein concentration, M = Fe^{2+} concentration and K_D = dissociation constant. (D) Extinction coefficient of Fe(II)-M121H/H46EAz at 330 nm is determined by fitting the plot of Abs at 330 nm vs. Fe^{2+} concentration using Beer's law $A = \varepsilon l c$ where $l = 1$ cm and c = Fe^{2+} concentration.

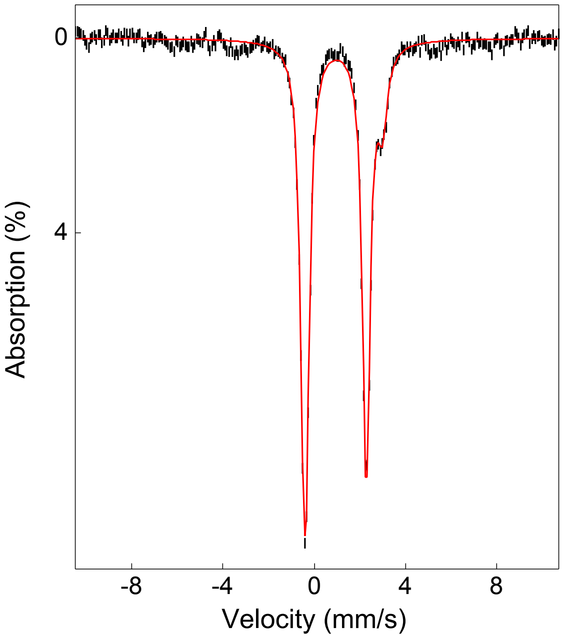

Fig. S3 | 4.2 K zero field Mössbauer spectrum of ^{57}Fe(II)-M121H/H46EAz (black) and the spectral simulation (red). The simulated parameters of two quadrupole doublets: δ_1 = 0.94 mm/s, $|\Delta E_{Q1}|$ = 2.66 mm/s, area =86%; δ_2 = 1.23 mm/s, $|\Delta E_{Q2}|$ = 3.55 mm/s, area =14%.

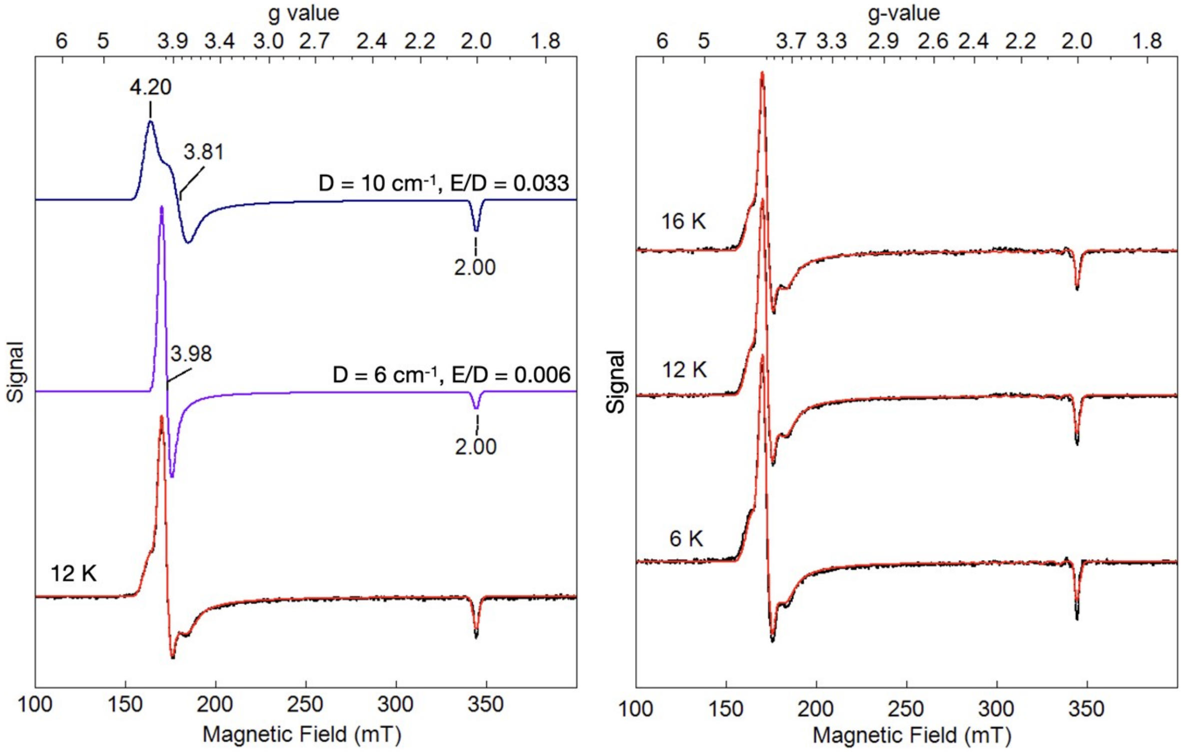

Figure S4. X-band EPR spectra of {FeNO}^{7} and the spectral simulations. Left panel: the experimental spectrum (black), the overall simulation (red), and two S = 3/2 component simulations (blue and purple). The zero-field splitting parameters are listed in the figure. Right panel, the experimental spectra (black) and the overall simulations (red) on the data collected under various temperatures indicated in the figure. These simulations were used to determine the axial zero field splitting parameter, D, for each S = 3/2 species shown in the spectra.

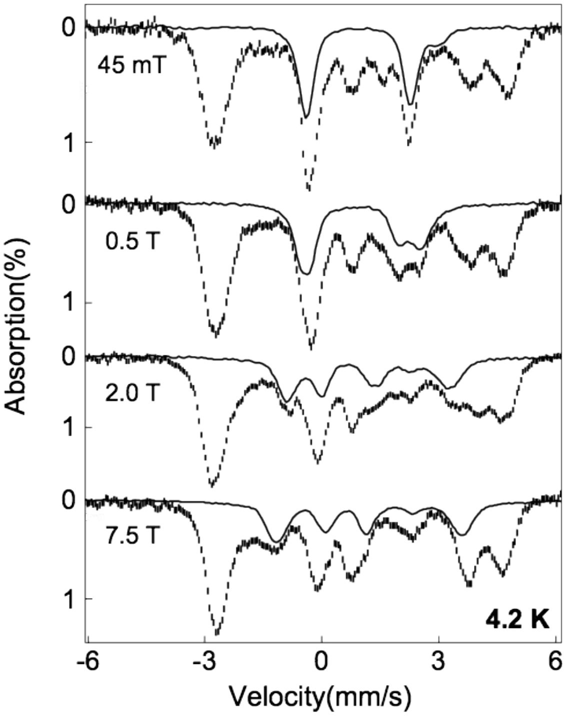

Fig. S5 | 4.2 K variable field Mössbauer spectra of {FeNO}^{7}. The spectra of Fe(II)-M121H/H46EAz complex (0.9 mM) treated with 0.7 eq. NO (black hash lines) and the Fe(II)-M121H/H46EAz complex scaled to 20% of the absorption area of the NO treated spectra (black solid lines).

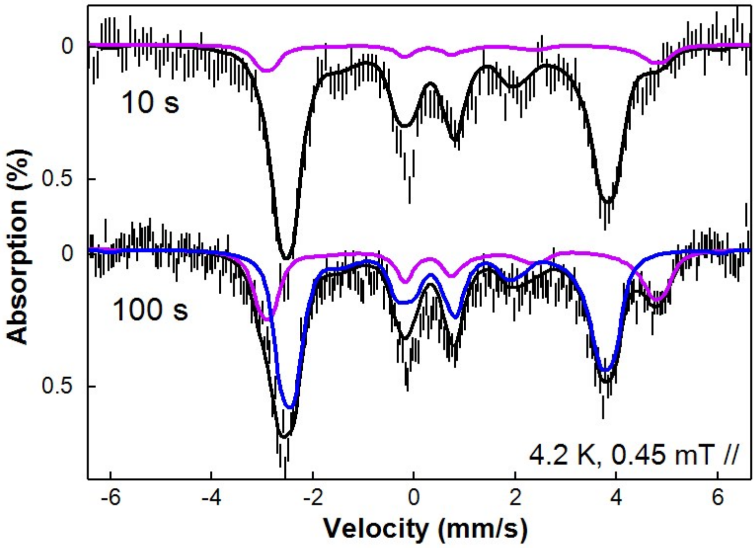

Fig. S6. 4.2 K Mössbauer spectra of the Fe(II)-M121H/H46EAz complex (0.9 mM) reacted with NO saturated buffer at different times. The spectrum measured on a sample quenched at 10 s is shown at the top (black hash line), the corresponding simulation (black) including the axial $\{FeNO\}^7$ species (~ 90%) and the rhombic $\{FeNO\}^7$ species (< 10%, purple line). The spectrum measured on a sample quenched at 100 s is shown at the bottom (black hash line), the corresponding simulation (black) including the axial $\{FeNO\}^7$ species (~ 70%, blue line) and the rhombic $\{FeNO\}^7$ species (~ 30%, purple line).

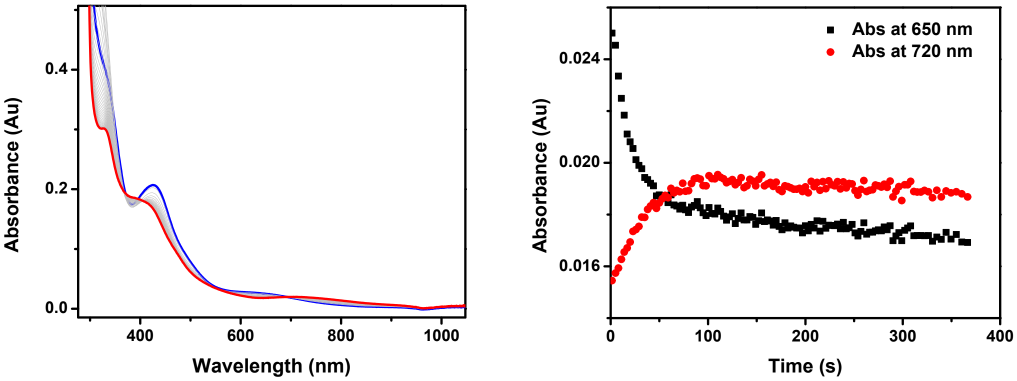

Fig. S7 | UV-Vis spectrum characterization of dinitrosyl iron complexes formation in engineered non heme iron site in Az. (A) Kinetic UV-Vis spectra of $\{FeNO\}^7$ being reduced with 1 *eq.* dithionite in the presence of excess amount of NO. UV-Vis spectra of isolated $\{FeNO\}^7$ species (blue) and $\{Fe(NO)_2\}^9$ species (red). (B) The time traces of absorbance at 650 nm (black) and 720 nm (red).

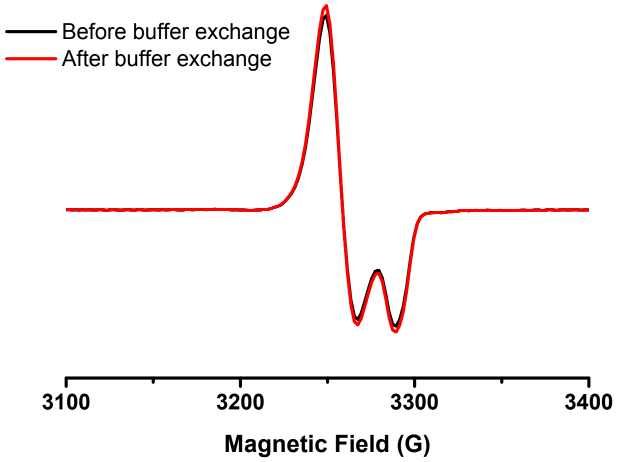

Fig. S8 | The EPR spectra of {Fe(NO)$_2$}^{9} species after three times buffer exchange using Amicon® Ultra-4 centrifugal filter devices with a 10 kDa molecular weight cutoff.

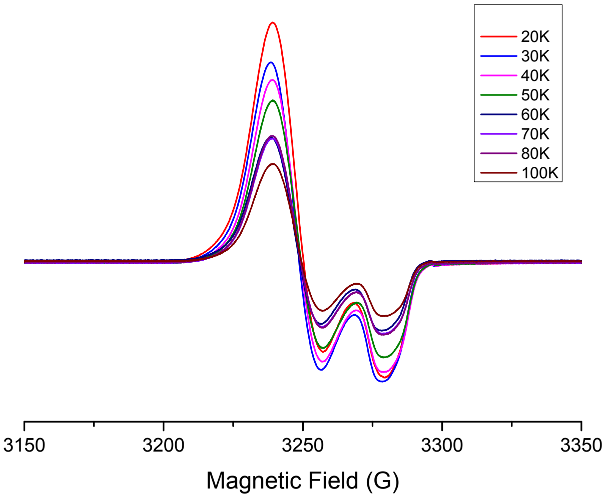

Fig. S9 | The EPR spectra of the {Fe(NO)$_2$}^{9} under different temperature.

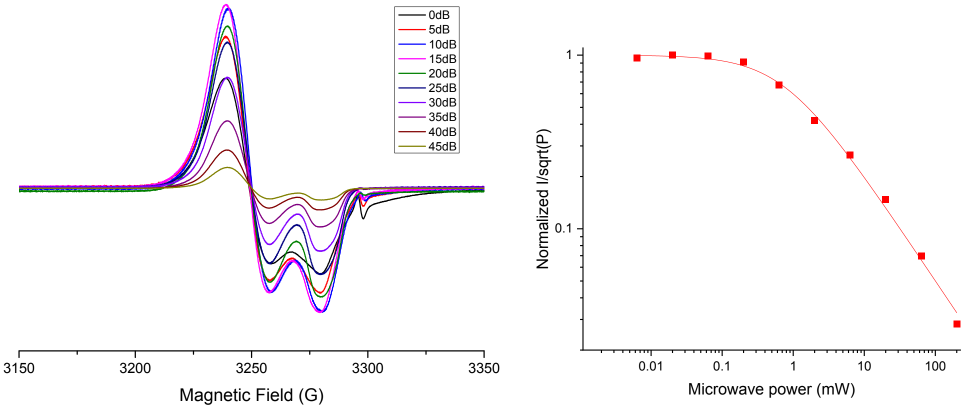

Fig. S10 | EPR power saturation study of the $\{Fe(NO)_2\}^9$ species. (A) EPR spectra of the $\{Fe(NO)_2\}^9$ species in 50 mM BisTris pH 7, recorded at 30 K under varying microwave power from 0 dB to 45 dB. Microwave frequency = 9.244 GHz, modulation amplitude = 2 G. (B) Plots of intensity/$\sqrt{P}$ vs. microwave power (mW) of the sharpest peak at g ~ 2.04. The plot is analyzed by using the equation:

$$\frac{I}{\sqrt{P}} = \frac{K}{[1 + (2^{\left(\frac{2}{B}\right)} - 1) \times (\frac{P}{P_{1/2}})]^{\frac{b}{2}}}$$

where I = peak intensity, K = constant, P = microwave power in mW, b = measure of homogeneity of the line shape with a value varying between 1 and 3, $P_{1/2}$ is the microwave frequency power at which the amplitude of the EPR signal is one-half of its unsaturated value.

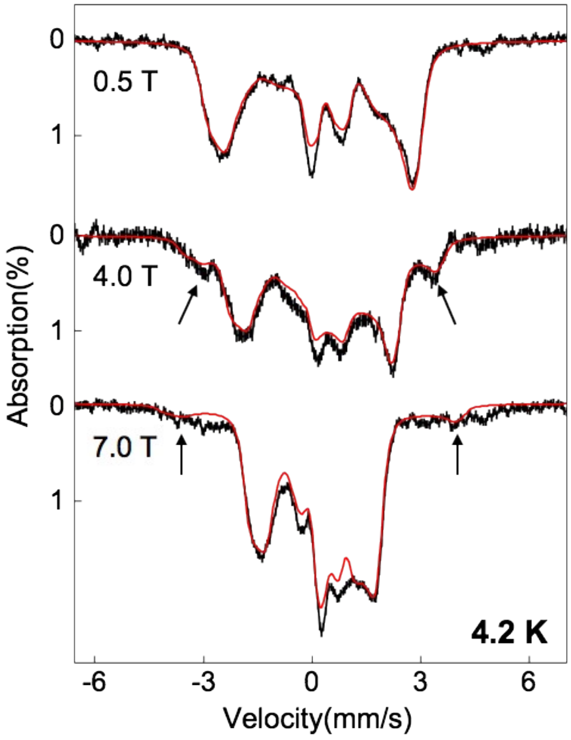

Fig. S11 | 4.2 K variable field Mössbauer spectra of $\{Fe(NO)_2\}^9$. The spectra of $\{Fe(NO)_2\}^9$ species are shown in black and the spectral simulation are in red. The arrows indicate the spectral features belong to the subspectra originated from the spin-up sub-level of the S = 1/2 spin system. The spectral component representing 30% of the Fe(II)-M121H/H46EAz complex was removed, see Fig. S12.

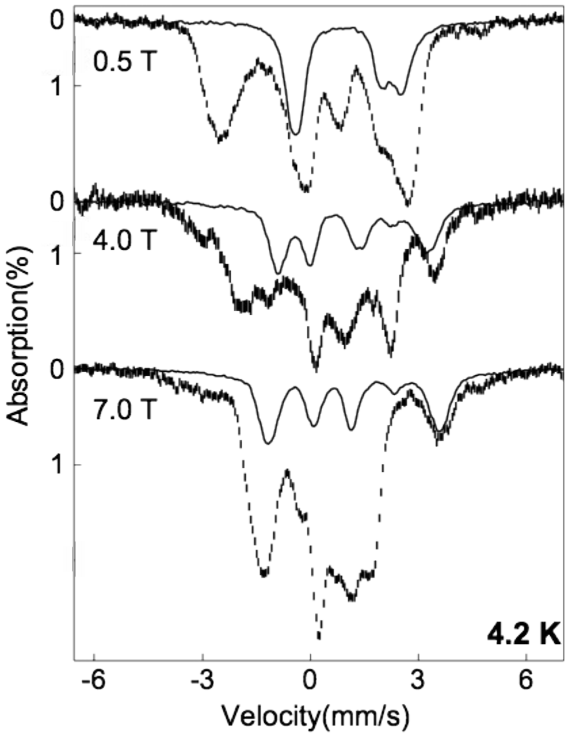

Fig. S12 | 4.2 K variable field Mössbauer spectra of the sample enriched with $\{Fe(NO)_2\}^9$ species. The spectra of the $\{Fe(NO)_2\}^9$ species scaled to 70 % of the absorption area (black hash lines) and the spectra of Fe(II)-M121H/H46EAz scaled to 30% of absorption area (black solid lines).

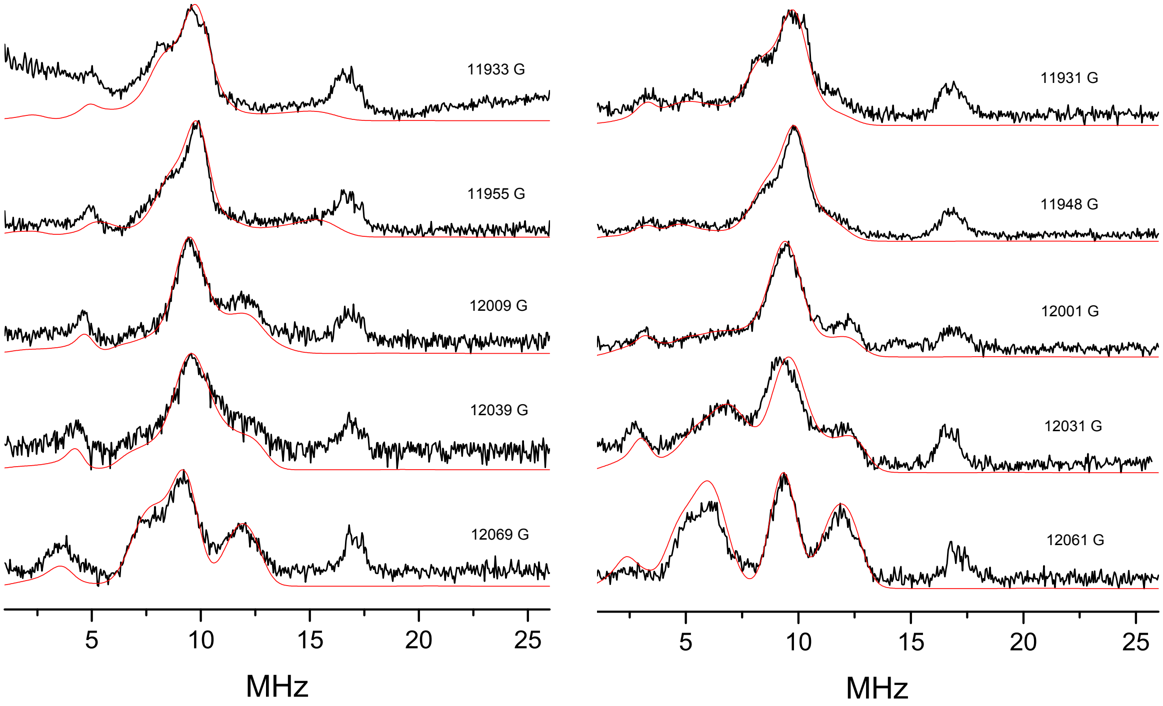

Fig. S13 | N-ENDOR investigation of dinitrosyl iron species formed in engineered non heme iron Az. (A) Q-band ^{14}N-ENDOR spectra of $\{Fe(NO)_2\}^9$ species collected at different magnetic fields at 30 K (black). The simulated spectra were shown in red. (B) Q-band ^{15}N-ENDOR spectra of $\{Fe(^{15}NO)_2\}^9$ species collected at different magnetic fields at 30 K. The simulated spectra were shown in red.

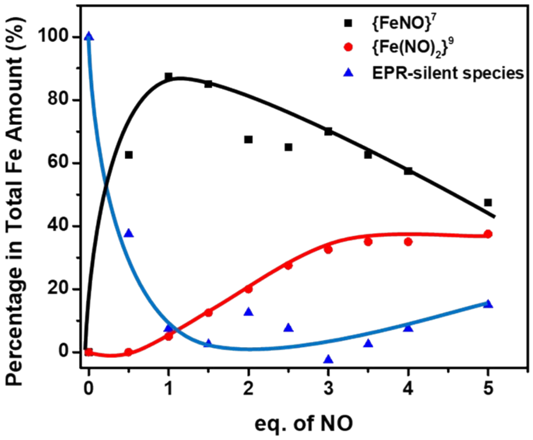

Fig. S14 | The NO dependent spin concentrations of various EPR active species. Black: overall of the two $\{FeNO\}^7$ species; Red: the S = 1/2 $\{Fe(NO)_2\}^9$ species; Blue: the percentage of EPR-silent species by subtracting the concentrations of $\{FeNO\}^7$ and $\{Fe(NO)_2\}^9$ from the total spin concentration.

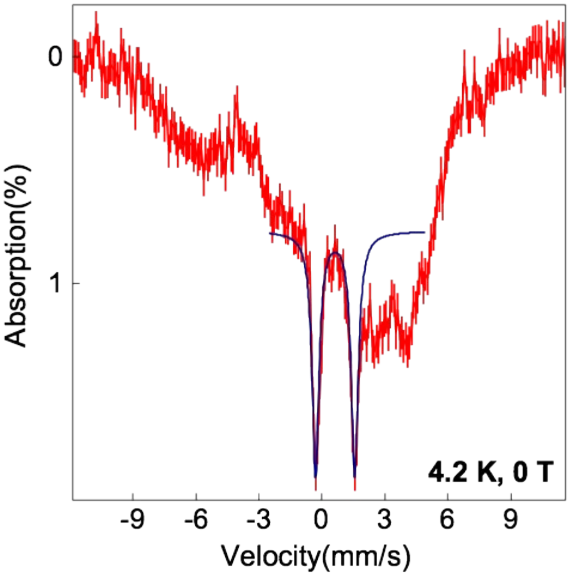

Fig. S15 | 4.2 K zero field Mössbauer spectrum of a NONOate treated Fe(II)-M121H/H46EAz complex illustrating the existence of {FeNO}8 species. Red: experimental spectrum; Blue: the spectral simulation of the $\{FeNO\}^8$ species with δ = 0.66 mm/s, $|\Delta E_Q|$ = 1.82 mm/s.

A

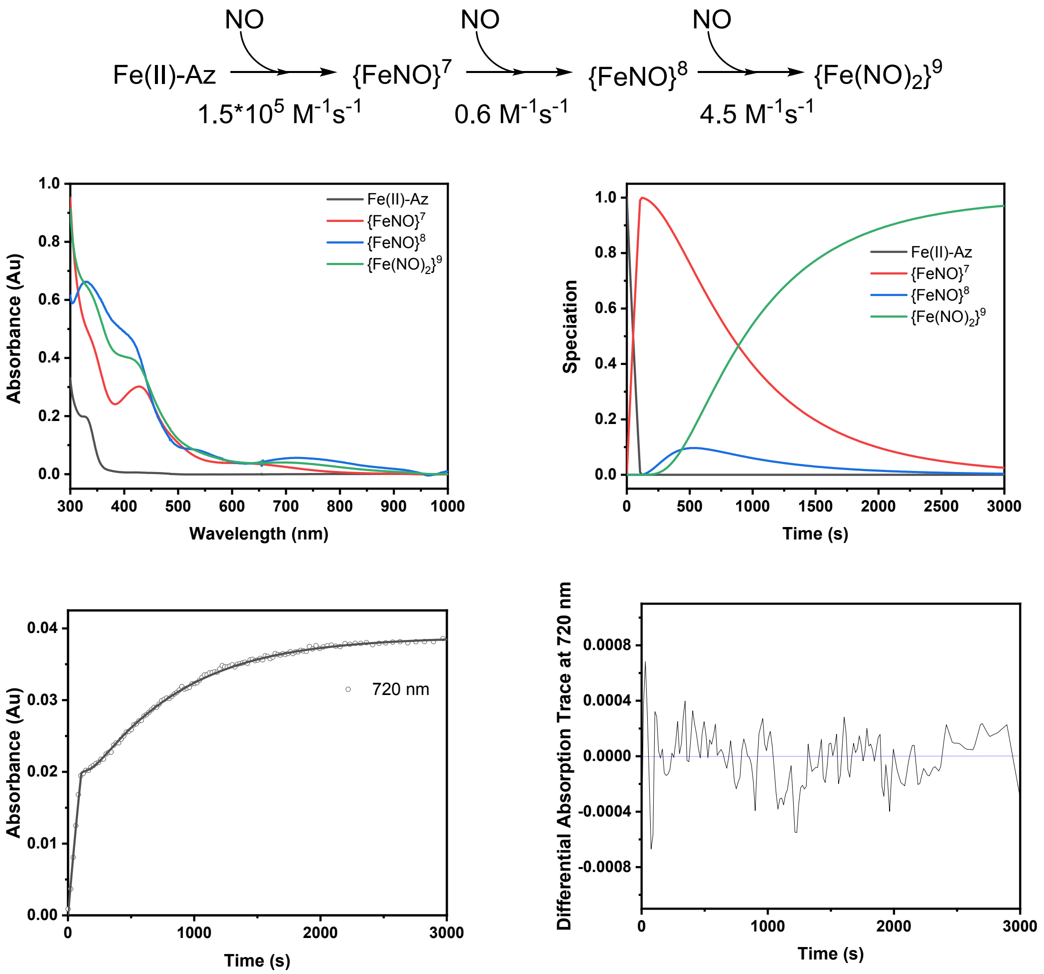
NO
NO
NO
Fe(II)-Az
{FeNO}^{7}
{FeNO}^{8}
{Fe(NO)$_2$}^{9}
1.5*10^5 M^{-1}s^{-1}
0.6 M^{-1}s^{-1}
4.5 M^{-1}s^{-1}
Absorbance (Au)
Wavelength (nm)
300
400
500
600
700
800
900
1000
0.0
0.2
0.4
0.6
0.8
1.0
Fe(II)-Az
{FeNO}^{7}
{FeNO}^{8}
{Fe(NO)$_2$}^{9}
Speciation
Time (s)
0
500
1000
1500
2000
2500
3000
Absorbance (Au)
0.00
0.01
0.02
0.03
0.04
720 nm
Time (s)
Differential Absorption Trace at 720 nm
-0.0008
-0.0004
0.0000
0.0004
0.0008

B

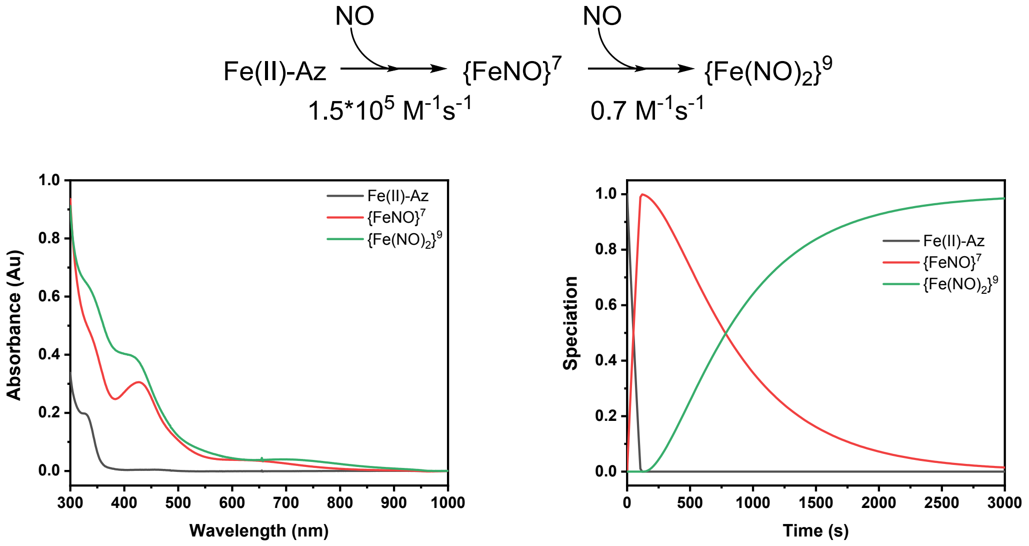
NO
NO
Fe(II)-Az
{FeNO}^{7}
{Fe(NO)$_2$}^{9}
1.5*10^5 M^{-1}s^{-1}
0.7 M^{-1}s^{-1}
Absorbance (Au)
Wavelength (nm)
300
400
500
600
700
800
900
1000
0.0
0.2
0.4
0.6
0.8
1.0
Fe(II)-Az
{FeNO}^{7}
{Fe(NO)$_2$}^{9}
Speciation
Time (s)
0
500
1000
1500
2000
2500
3000

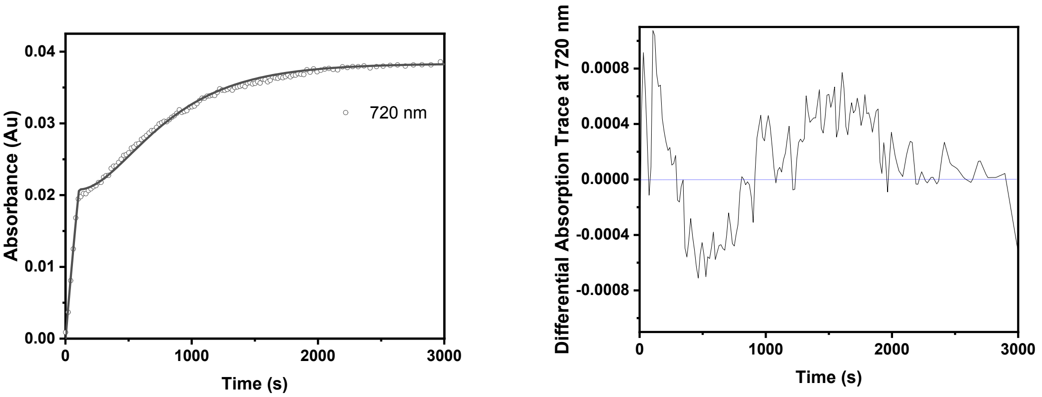

Fig. S16 | Spectral analysis of time-dependent optical absorption spectra shown in Figure 2 using single value decomposition (SVD) method. (A) Model that includes $\{FeNO\}^8$ species as an intermediate. (B) Model that excludes $\{FeNO\}^8$ as an intermediate. The identified spectra from SVD, time-dependent speciation, the experimental and simulated time traces at 720 nm, and differential absorption trace at 720nm are plotted respectively.

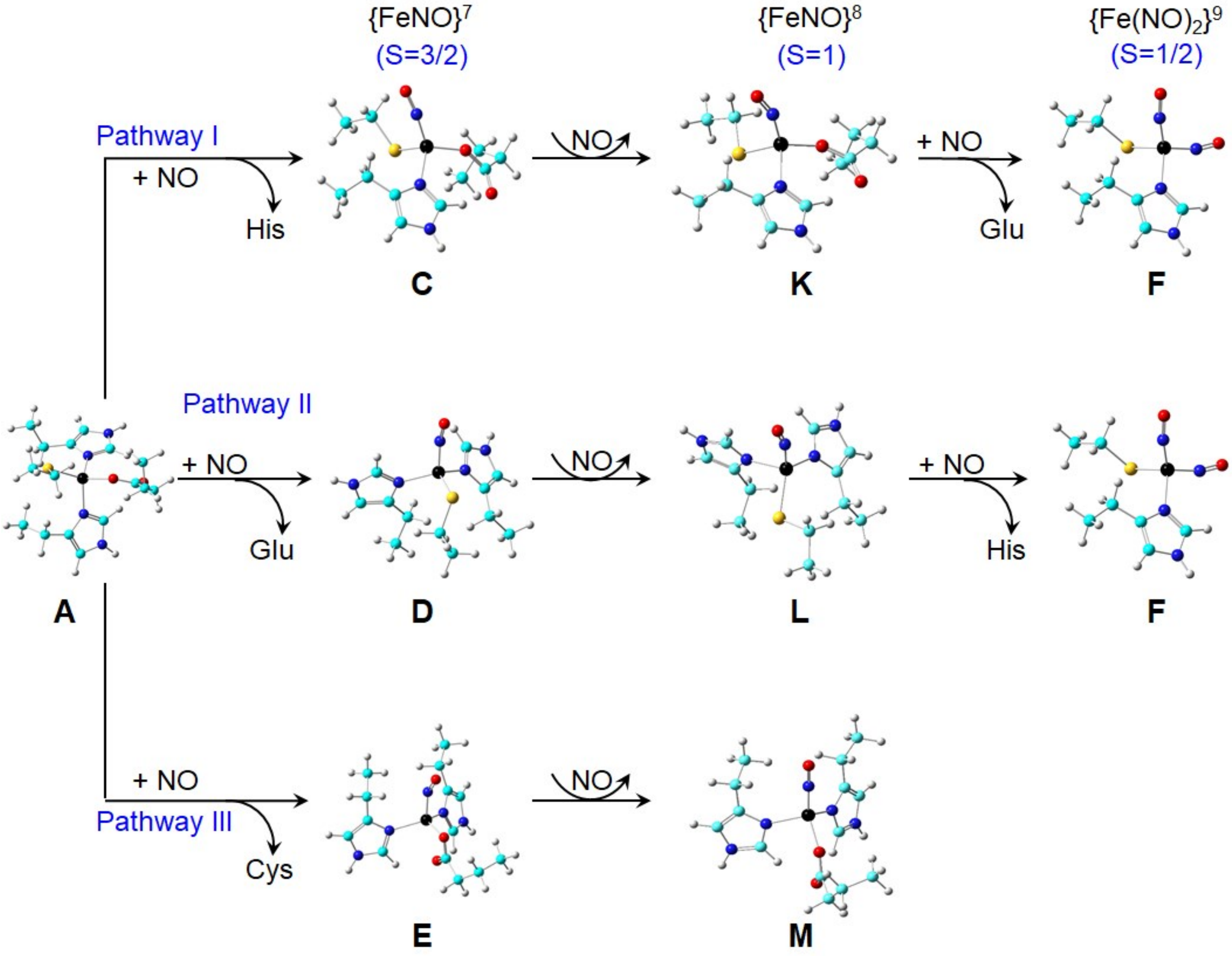

Fig. S17 | Possible reaction pathways. Color scheme: C – cyan, Fe – black, N – blue, O – red, S – yellow, H – grey.

Table S1. Spin Hamiltonian parameters of the various observed iron-nitrosyl complexes.[a]

Species	$\{FeNO\}^7$		$\{FeNO\}^8$	$\{FeNO\}^{8'}$	$\{Fe(NO)_2\}^9$
S	3/2	3/2	-	-	1/2
D (cm^{-1})	10 (1)	6 (1)	-	-	-
E/D	0.033(3)	0.007(2)	-	-	-
g	[2.024, 2.024, 2.00]	[2.012 2.012 2.00]	-	-	[2.040, 2.034, 2.012]
δ (mm/s)	0.60(2)	0.47(2)	0.66(1)	0.77(1)	0.26
ΔE_Q (mm/s)	-1.60(5)	-1.00(5)	1.82(2) [b]	2.20(2) [b]	0.83
η	0	1.2	-	-	0.9
$[A_x\ A_y\ A_z]/g_n\beta_n$ (T)	[-22.0(5), -23.0(5), -30(2)]	[-19.2(5), -19.0(5), -25(5)]	-	-	[-36.5(5), -31.8(5), -10(1)]
α β γ (degree) [c]	-	-	-	-	70, 25, 0

a the numerical values in the parentheses indicate the uncertainty of the last digit of the entry.
b The sign of ΔE_Q is not determined
c The y-z-y convention is used for the definition of Euler angles

Table S2 | The simulation parameters for the ^{14}N-ENDOR fittings.

	x	y	z	α	β	γ
A (^{14}N His)	9.7	11.1	15.3	16	32	-19
Q (^{14}N His)	0.59	0.42	-1.01	8	20	2
A(^{14}N NO)	0.5	3.5	15.7	109	-95	-114
Q (^{14}N NO)	-0.01	0.54	-0.53	110	-94	-101
A(^{14}N NO)	0.5	3.5	15.7	-109	-95	114
Q (^{14}N NO)	-0.01	0.54	-0.53	-110	-94	101
g	2.040	2.034	2.012			

Note:
1) Hyperfine and quadrupole coupling in MHz. For ^{15}N hyperfine couplings, multiply by 1.402.
2) Euler angles rotate the diagonal A matrix into the coordinate system in which g is diagonal. The Euler angles that diagonalize A are given by -γ, β, -α.
3) The coupling matrixes for the two NO's are assumed to be symmetric about the yz plane.

Table S3. Vibrational frequencies (in cm^{-1}) of the $\{FeNO\}^7$ and $\{Fe(NO)_2\}^9$ species.

	ν(Fe-S$_{Cys}$) (Δ^{15}N)	ν(Fe-NO) (Δ^{15}N)	δ(Fe-N-O) (Δ^{15}N)	ν(N-O) (Δ^{15}N)	References
M121H/H46EAz $\{FeNO\}^7$	**362/394 (0)**	**519 (-3)**	**535 (-18)**	**1795 (-32)**	**This work**
Superoxide reductase $\{FeNO\}^7$	291 (0)	475 (-7)		1721 (-31)	[42]
R2-RNR $\{FeNO\}^7$		445(-7)	434 (-9)	1742 (-29)	[43]
M121H/H46EAz $\{Fe(NO)_2\}^9$	**360 (0)**	**534 (-6), 594 (-6)**	**423 (-12)**	**1781 (-32), 1724**	**This work**
Ferric uptake regulator $\{Fe(NO)_2\}^9$				1762 (-32), 1715 (-27)	[44]
R2-RNR $\{Fe(NO)_2\}^9$				1761, 1785	[43]
$[(SPh)_2\{Fe(NO)_2\}^9]^-$		525 (-6), 598 (-4)	440 (-11)	1731 (-37), 1692 (-31)	[45]

Table S4. Spin concentrations of various species observed in EPR (units: mM)

eq. of NO*	$\{FeNO\}^7$ S= 3/2		$\{Fe(NO)_2\}^9$ S = ½	**Total**
	E/D = 0.033	E/D = 0.006		
0.5	0.14	0.11	0.00	**0.25**
1	0.20	0.15	0.02	**0.37**
1.5	0.18	0.15	0.04	**0.37**
2	0.14	0.12	0.08	**0.34**
2.5	0.13	0.12	0.11	**0.36**
3	0.13	0.13	0.13	**0.39**
3.5	0.11	0.13	0.14	**0.38**
4	0.10	0.12	0.14	**0.36**
5	0.08	0.11	0.16	**0.35**
3 + 2 *eq.* NaDT	~ 0	~ 0.005	0.30	**0.30**

* Assuming each Proli NONOate molecule gives 2 molecules of NO.

Table S5. Reaction Energies in Different Pathways Shown in Fig. S17 (Unit: kcal/mol).

Pathway	Step	ΔE	ΔE$_{ZPE}$	ΔH	ΔG
I	**A→C**	-32.06	-29.11	-28.74	-33.30
	C→K a)	0.00	0.00	0.00	0.00
	K→F	-34.35	-30.65	-30.98	-33.03
II	**A→D**	-12.54	-9.66	-9.26	-13.56
	D→L a)	10.73	10.69	10.79	10.20
	L→F	-45.08	-41.34	-41.77	-43.23
III	**A→E**	-12.94	-9.38	-9.31	-11.51
	E→M a)	6.00	6.85	6.56	9.31

a) As the detailed NO reduction in this $\{FeNO\}^7$ to $\{FeNO\}^8$ process needs further study, here the relative reaction energies of this step in the three pathways were calculated with respect to the Pathway I **C→K** step, assuming the same fate for the oxidized NO in this step of reaction.

Table S6. Comparison of Calculated Spectroscopic Properties and Spin Densities from the First-sphere and Second-sphere Models for a $\{FeNO\}^7$ system

Model	System	S	δ_{Fe} (mm/s)	ΔE_Q (mm/s)	ν_{NO} (cm^{-1})	$\rho_{\alpha\beta}^{Fe}$ (e)	$\rho_{\alpha\beta}^{NO}$ (e)
D	$Fe(NO)(His)_2(Cys)$	3/2	0.44	0.68	1820	3.426	-0.946
D'	2nd sphere model [a)]	3/2	0.42	0.57	1813	3.468	-0.963

[a)] The three residues that have backbone moieties H-bonded to the first sphere residues are included, using the short models of CH_3**NH**CHO to represent the N-H…S hydrogen bonds with Cys from F114 and N47, and CH_3C**O**NH_2 to represent the O(M13)…H-Nε(H121) hydrogen bond. Heave atoms in these backbone models are fixed in the x-ray structure positions along with the Cα atoms of first sphere residues to mimic the protein environment effect during geometry optimization. The optimized structure is shown below. After optimization, the H121…M13 interaction is strengthened as indicated by a shorted N…O distance from 3.02 Å to 2.69 Å, and the N47…C112 interaction is not significantly changed (the N…S distance is 3.56 Å, similar to 3.48 Å in the original x-ray structure), while the F114…C112 interaction is lost because the N…S distance is changed from 3.47 Å to 4.80 Å.

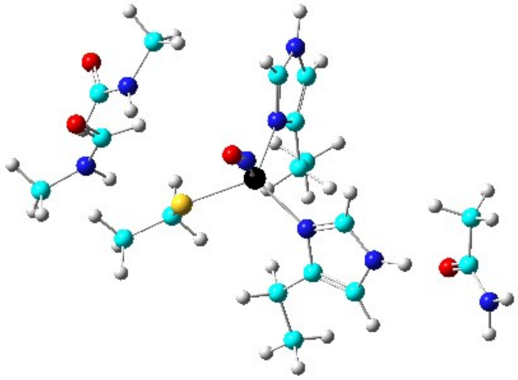

References:

1. Sieracki, N. A.; Tian, S.; Hadt, R. G.; Zhang, J.-L.; Woertink, J. S.; Nilges, M. J.; Sun, F.; Solomon, E. I.; Lu, Y., Copper–sulfenate complex from oxidation of a cavity mutant of Pseudomonas aeruginosa azurin. *Proc. Natl. Acad. Sci. U.S.A.* **2014,** *111* (3), 924-929.
2. Johnson, K. A.; Simpson, Z. B.; Blom, T., Global Kinetic Explorer: A new computer program for dynamic simulation and fitting of kinetic data. *Anal. Biochem.* **2009,** *387* (1), 20-29.
3. Johnson, K. A.; Simpson, Z. B.; Blom, T., FitSpace Explorer: An algorithm to evaluate multidimensional parameter space in fitting kinetic data. *Anal. Biochem.* **2009,** *387* (1), 30-41.
4. Henry, E. R.; Hofrichter, J., Singular value decomposition: Application to analysis of experimental data. In *Methods Enzymol.*, Academic Press: 1992; Vol. 210, pp 129-192.
5. Petasis, D. T.; Hendrich, M. P., Chapter Eight - Quantitative Interpretation of Multifrequency Multimode EPR Spectra of Metal Containing Proteins, Enzymes, and Biomimetic Complexes. In *Methods Enzymol.*, Qin, P. Z.; Warncke, K., Eds. Academic Press: 2015; Vol. 563, pp 171-208.
6. Zhang, Y.; Mao, J.; Godbout, N.; Oldfield, E., Mössbauer Quadrupole Splittings and Electronic Structure in Heme Proteins and Model Systems: A Density Functional Theory Investigation. *J. Am. Chem. Soc.* **2002,** *124* (46), 13921-13930.
7. Zhang, Y.; Mao, J.; Oldfield, E., ^{57}Fe Mössbauer Isomer Shifts of Heme Protein Model Systems: Electronic Structure Calculations. *J. Am. Chem. Soc.* **2002,** *124* (26), 7829-7839.
8. Becke, A. D., Density‐functional thermochemistry. III. The role of exact exchange. *J. Chem. Phys.* **1993,** *98* (7), 5648-5652.
9. Wachters, A. J. H., Gaussian Basis Set for Molecular Wavefunctions Containing Third‐Row Atoms. *J. Chem. Phys.* **1970,** *52* (3), 1033-1036.
10. Zhang, Y.; Oldfield, E., An Investigation of the Unusual ^{57}Fe Mössbauer Quadrupole Splittings and Isomer Shifts in 2 and 3-Coordinate Fe(II) Complexes. *J. Phys. Chem. B* **2003,** *107* (29), 7180-7188.
11. Ling, Y.; Zhang, Y., Mössbauer, NMR, Geometric, and Electronic Properties in S = 3/2 Iron Porphyrins. *J. Am. Chem. Soc.* **2009,** *131* (18), 6386-6388.
12. Zhang, Y.; Oldfield, E., On the Mössbauer Spectra of Isopenicillin N Synthase and a Model $\{FeNO\}^7$ (S = 3/2) System. *J. Am. Chem. Soc.* **2004,** *126* (31), 9494-9495.
13. Zhang, Y.; Oldfield, E., Cytochrome P450: An Investigation of the Mössbauer Spectra of a Reaction Intermediate and an Fe(IV)=O Model System. *J. Am. Chem. Soc.* **2004,** *126* (14), 4470-4471.
14. Zhang, Y.; Gossman, W.; Oldfield, E., A Density Functional Theory Investigation of Fe−N−O Bonding in Heme Proteins and Model Systems. *J. Am. Chem. Soc.* **2003,** *125* (52), 16387-16396.
15. Zhang, Y.; Oldfield, E., ^{57}Fe Mössbauer Quadrupole Splittings and Isomer Shifts in Spin-Crossover Complexes: A Density Functional Theory Investigation. *J. Phys. Chem. A* **2003,** *107* (20), 4147-4150.
16. Ling, Y.; Davidson, V. L.; Zhang, Y., Unprecedented Fe(IV) Species in a Diheme Protein MauG: A Quantum Chemical Investigation on the Unusual Mössbauer Spectroscopic Properties. *J. Phys. Chem. Lett.* **2010,** *1* (19), 2936-2939.
17. Ling, Y.; Zhang, Y., Deciphering Structural Fingerprints for Metalloproteins with Quantum Chemical Calculations. *Annu. Rep. Comput. Chem.* **2010,** *6*, 64-77.
18. Katigbak, J.; Zhang, Y., Iron Binding Site in a Global Regulator in Bacteria–Ferric Uptake Regulator (Fur) Protein: Structure, Mössbauer Properties, and Functional Implication. *J. Phys. Chem. Lett.* **2012,** *3* (23), 3503-3508.
19. Fu, R.; Gupta, R.; Geng, J.; Dornevil, K.; Wang, S.; Zhang, Y.; Hendrich, M. P.; Liu, A., Enzyme Reactivation by Hydrogen Peroxide in Heme-based Tryptophan Dioxygenase. *J. Biol. Chem.* **2011,** *286* (30), 26541-26554.
20. Dufek, P.; Blaha, P.; Schwarz, K., Determination of the Nuclear Quadrupole Moment of 57Fe. *Phys. Rev. Lett.* **1995,** *75* (19), 3545-3548.
21. Frisch, M. J.; Trucks, G. W.; Schlegel, H. B.; Scuseria, G. E.; Robb, M. A.; Cheeseman, J. R.; Scalmani, G.; Barone, V.; Mennucci, B.; Petersson, G. A.; Nakatsuji, H.; Caricato, M.; Li, X.; Hratchian, H. P.; Izmaylov, A. F.; Bloino, J.; Zheng, G.; Sonnenberg, J. L.; Hada, M.; Ehara, M.; Toyota, K.; Fukuda, R.; Hasegawa, J.; Ishida, M.; Nakajima, T.; Honda, Y.; Kitao, O.; Nakai, H.; Vreven, T.; Montgomery, J. A.; Peralta, J. E.; Ogliaro, F.; Bearpark, M.; Heyd, J. J.; Brothers, E.; Kudin, K. N.; Staroverov, V. N.; Kobayashi, R.; Normand, J.; Raghavachari, K.; Rendell, A.; Burant, J. C.; Iyengar, S. S.; Tomasi, J.; Cossi, M.; Rega, N.; Millam, J. M.; Klene, M.; Knox, J. E.; Cross, J. B.; Bakken, V.; Adamo, C.; Jaramillo, J.; Gomperts, R.; Stratmann, R. E.; Yazyev, O.; Austin, A. J.; Cammi, R.; Pomelli, C.; Ochterski, J. W.; Martin, R. L.; Morokuma, K.; Zakrzewski, V. G.; Voth, G. A.; Salvador, P.; Dannenberg, J. J.;

Dapprich, S.; Daniels, A. D.; Farkas; Foresman, J. B.; Ortiz, J. V.; Cioslowski, J.; Fox, D. J., Gaussian 09, Revision B.01. Wallingford CT, 2009.

22. Biegler–König;, F.; Schönbohm;, J.; Bayles., D., AIM2000—A Program to Analyze and Visualize Atoms in Molecules. *J. Comput. Chem.* **2001,** *22* (5), 545-559.

23. Bhagi-Damodaran, A.; Michael, M. A.; Zhu, Q. H.; Reed, J.; Sandoval, B. A.; Moënne-Loccoz, P.; Zhang, Y.; Lu, Y., Why is copper preferred over iron for oxygen activation and reduction in haem-copper-oxidases. *Nature Chemistry* **2017,** *9*, 257-263.

24. Yang, L.; Ling, Y.; Zhang, Y., HNO Binding in a Heme Protein: Structures, Spectroscopic Properties, and Stabilities. *J. Am. Chem. Soc.* **2011,** *133* (35), 13814-13817.

25. Span, I.; Wang, K.; Eisenreich, W.; Bacher, A.; Zhang, Y.; Oldfield, E.; Groll, M., Insights into the Binding of Pyridines to the Iron–Sulfur Enzyme IspH. *J. Am. Chem. Soc.* **2014,** *136* (22), 7926-7932.

26. Sumner, S.; Söderhjelm, P.; Ryde, U., Effect of Geometry Optimizations on QM-Cluster and QM/MM Studies of Reaction Energies in Proteins. *J. Chem. Theory Comput.* **2013,** *9* (9), 4205-4214.

27. Martin-Diaconescu, V.; Chacón, K. N.; Delgado-Jaime, M. U.; Sokaras, D.; Weng, T.-C.; DeBeer, S.; Blackburn, N. J., Kβ Valence to Core X-ray Emission Studies of Cu(I) Binding Proteins with Mixed Methionine – Histidine Coordination. Relevance to the Reactivity of the M- and H-sites of Peptidylglycine Monooxygenase. *Inorg. Chem.* **2016,** *55* (7), 3431-3439.

28. Prejanò, M.; Marino, T.; Russo, N., How Can Methanol Dehydrogenase from Methylacidiphilum fumariolicum Work with the Alien CeIII Ion in the Active Center? A Theoretical Study. *Chem. Eur. J.* **2017,** *23* (36), 8652-8657.

29. Huang, H.-T.; Dillon, S.; Ryan, K. C.; Campecino, J. O.; Watkins, O. E.; Cabelli, D. E.; Brunold, T. C.; Maroney, M. J., The Role of Mixed Amine/Amide Ligation in Nickel Superoxide Dismutase. *Inorg. Chem.* **2018,** *57* (20), 12521-12535.

30. Bertarello, A.; Benda, L.; Sanders, K. J.; Pell, A. J.; Knight, M. J.; Pelmenschikov, V.; Gonnelli, L.; Felli, I. C.; Kaupp, M.; Emsley, L.; Pierattelli, R.; Pintacuda, G., Picometer Resolution Structure of the Coordination Sphere in the Metal-Binding Site in a Metalloprotein by NMR. *J. Am. Chem. Soc.* **2020,** *142* (39), 16757-16765.

31. Becke, A. D., Density-functional exchange-energy approximation with correct asymptotic behavior. *Phys. Rev. A* **1988,** *38* (6), 3098-3100.

32. Perdew, J. P.; Burke, K.; Wang, Y., Generalized gradient approximation for the exchange-correlation hole of a many-electron system. *Phys. Rev. B* **1996,** *54* (23), 16533-16539.

33. Li, J.; Wang, K.; Smirnova, T. I.; Khade, R. L.; Zhang, Y.; Oldfield, E., Isoprenoid Biosynthesis: Ferraoxetane or Allyl Anion Mechanism for IspH Catalysis? *Angew. Chem. Int. Ed.* **2013,** *52* (25), 6522-6525.

34. Liu, Y.-L.; Guerra, F.; Wang, K.; Wang, W.; Li, J.; Huang, C.; Zhu, W.; Houlihan, K.; Li, Z.; Zhang, Y.; Nair, S. K.; Oldfield, E., Structure, function and inhibition of the two- and three-domain 4Fe-4S IspG proteins. *Proc. Natl. Acad. Sci. U.S.A.* **2012,** *109* (22), 8558-8563.

35. Wang, K.; Wang, W.; No, J.-H.; Zhang, Y.; Zhang, Y.; Oldfield, E., Inhibition of the Fe_4S_4-Cluster-Containing Protein IspH (LytB): Electron Paramagnetic Resonance, Metallacycles, and Mechanisms. *J. Am. Chem. Soc.* **2010,** *132* (19), 6719-6727.

36. Chakraborty, S.; Reed, J.; Ross, M.; Nilges, M. J.; Petrik, I. D.; Ghosh, S.; Hammes-Schiffer, S.; Sage, J. T.; Zhang, Y.; Schulz, C. E.; Lu, Y., Spectroscopic and Computational Study of a Nonheme Iron Nitrosyl Center in a Biosynthetic Model of Nitric Oxide Reductase. *Angew. Chem. Int. Ed.* **2014,** *53* (9), 2417-2421.

37. Mennucci, B.; Tomasi, J., Continuum solvation models: A new approach to the problem of solute's charge distribution and cavity boundaries. *J. Chem. Phys.* **1997,** *106* (12), 5151-5158.

38. Blachly, P. G.; Sandala, G. M.; Giammona, D. A.; Bashford, D.; McCammon, J. A.; Noodleman, L., Broken-Symmetry DFT Computations for the Reaction Pathway of IspH, an Iron–Sulfur Enzyme in Pathogenic Bacteria. *Inorg. Chem.* **2015,** *54* (13), 6439-6461.

39. Chai, J.-D.; Head-Gordon, M., Long-range corrected hybrid density functionals with damped atom–atom dispersion corrections. *Phys. Chem. Chem. Phys.* **2008,** *10* (44), 6615-6620.

40. Tonzetich, Z. J.; Do, L. H.; Lippard, S. J., Dinitrosyl Iron Complexes Relevant to Rieske Cluster Nitrosylation. *J. Am. Chem. Soc.* **2009,** *131* (23), 7964-7965.

41. Tsai, F.-T.; Chen, P.-L.; Liaw, W.-F., Roles of the Distinct Electronic Structures of the $\{Fe(NO)_2\}^9$ and $\{Fe(NO)_2\}^{10}$ Dinitrosyliron Complexes in Modulating Nitrite Binding Modes and Nitrite Activation Pathways. *J. Am. Chem. Soc.* **2010,** *132* (14), 5290-5299.

42. Clay, M. D.; Cosper, C. A.; Jenney, F. E.; Adams, M. W. W.; Johnson, M. K., Nitric oxide binding at the mononuclear active site of reduced Pyrococcus furiosus superoxide reductase. *Proc. Natl. Acad. Sci. U.S.A.* **2003,** *100* (7), 3796-3801.

43. Lu, S.; Libby, E.; Saleh, L.; Xing, G.; Bollinger, J. M.; Moënne-Loccoz, P., Characterization of NO adducts of the diiron center in protein R2 of Escherichia coli ribonucleotide reductase and site-directed variants; implications for the O2 activation mechanism. *J. Biol. Inorg. Chem.* **2004,** *9* (7), 818-827.

44. D'Autréaux, B.; Horner, O.; Oddou, J.-L.; Jeandey, C.; Gambarelli, S.; Berthomieu, C.; Latour, J.-M.; Michaud-Soret, I., Spectroscopic Description of the Two Nitrosyl−Iron Complexes Responsible for Fur Inhibition by Nitric Oxide. *J. Am. Chem. Soc.* **2004,** *126* (19), 6005-6016.

45. Dai, R. J.; Ke, S. C., Detection and Determination of the {Fe(NO)2} Core Vibrational Features in Dinitrosyl−Iron Complexes from Experiment, Normal Coordinate Analysis, and Density Functional Theory: An Avenue for Probing the Nitric Oxide Oxidation State. *J. Phys. Chem. B* **2007,** *111* (9), 2335-2346.